WOS URL:
https://www.webofscience.com/wos/author/record/JFK-3719-2023

Scopus URL:
https://www.scopus.com/authid/detail.uri?authorId=57190385237

ORCID URL:
https://orcid.org/0000-0001-7379-6597

Dr. Rufeng Zhang

Department of Pharmacology, Biocytogen Pharmaceuticals (Beijing) Co., Ltd., China

Research Interest:

obesity and diabetes; NAFLD/NASH; inflammatory disease; fibrosis; antibody discovery; humanized animal model

Bio Statement:

Rufeng Zhang is a pharmaceutical scientist currently working at Biocytogen Pharmaceuticals (Beijing) Co., Ltd. He completed his PhD training at Peking University from 2014 to 2019, during which time his work mainly focused on the association between mitochondrial proteins and metabolic diseases. After joining Biocytogen, he has focused on the building of disease animal models and their application in the evaluation of drug efficacy, such as dietary and chemically induced animal models, gene editing animal models, and their combined application in disease areas such as obesity, diabetes, NASH, inflammatory diseases, fibrosis and kidney diseases.

NDUFAB1 protects against obesity and insulin resistance by enhancing mitochondrial metabolism

Rufeng Zhang, Tingting Hou, Heping Cheng, Xianhua Wang*

State Key Laboratory of Membrane Biology, Beijing Key Laboratory of Cardiometabolic Molecular Medicine, Peking-Tsinghua Center for Life Sciences, Institute of Molecular Medicine, Peking University, Beijing 100871, China

*** Corresponding author:** Xianhua Wang, xianhua@pku.edu.cn

ABSTRACT

Mitochondria are fundamental organelles for cellular and systemic metabolism, and their dysfunction has been implicated in the development of diverse metabolic diseases. Boosted mitochondrial metabolism might be able to protect against metabolic stress and prevent metabolic disorders. Here we show that NADH: ubiquinone oxidoreductase (NDU)-FAB1, also known as mitochondrial acyl carrier protein, acts as a novel enhancer of mitochondrial metabolism and protects against obesity and insulin resistance. Mechanistically, NDUFAB1 coordinately enhances lipoylation and activation of pyruvate dehydrogenase mediated by the mitochondrial fatty acid synthesis pathway and increases the assembly of respiratory complexes and supercomplexes. Skeletal muscle–specific ablation of NDUFAB1 causes systemic disruption of glucose homeostasis and defective insulin signaling, leading to growth arrest and early death within 5 postnatal days. In contrast, NDUFAB1 overexpression effectively protects mice against obesity and insulin resistance when the animals are challenged with a high-fat diet. Our findings indicate that NDUFAB1 could be a novel mitochondrial target to prevent obesity and insulin resistance by enhancing mitochondrial metabolism.

Keywords: pyruvate dehydrogenase; mitochondrial respiratory complexes; respiratory supercomplexes; metabolic disorder

Type 2 diabetes is one of the most common metabolic diseases in the world, expected to affect almost a third of the population by 2050[1]. The rise in the prevalence of diabetes is closely associated with a significant rise of epidemic proportion in obesity, which is one of the major underlying causes of insulin resistance and a key component in the etiology of diabetes[2]. Disordered cellular metabolism is involved in the development of obesity.

Of paramount importance to cellular metabolism is energy transduction under the control of mitochondria. To transduce energy, the mitochondria consume oxygen to "burn" carbon intermediates derived from 3 principal nutrients: fatty acids, glucose, and amino acids[3]. The mitochondria switch between fuel sources in response to a host of cellular signals. It has been increasingly recognized, however, that nutrient overload and heightened substrate competition result in impaired fuel switching and energy dysregulation disorders[3]. Mitochondrial dysfunction has been shown to be closely associated with the development of insulin resistance that leads to type 2 diabetes[4,5]. Altered mitochondrial content or oxidative capacity has been found in insulin-responsive tissues of patients with insulin resistance[6–9]. Although the evidence for a causal relationship between mitochondrial dysfunction and insulin resistance is still weak, emerging evidence indicates that boosting mitochondrial function might be beneficial to improve insulin sensitivity and glucose homeostasis[5]. Therefore, identification of potential targets to enhance mitochondrial metabolism may provide a novel therapeutic strategy for obesity and insulin resistance.

ORIGINAL SOURCE

Zhang R, Hou T, Cheng H, Wang X. NDUFAB1 protects against obesity and insulin resistance by enhancing mitochondrial metabolism. *The FASEB Journal* 2019; 33(12): 13310–13322. doi: 10.1096/fj.201901117RR

NADH: ubiquinone oxidoreductase (NDU)-FAB1, also known as mitochondrial acyl carrier protein[10], plays a multifunctional role in mitochondria. It is an essential component of the mitochondrial fatty acid synthesis (mtFAS) pathway[11,12], which synthesizes lipoic acid, a cofactor required for a number of mitochondrial enzymes including pyruvate dehydrogenase (PDH), aketoglutarate dehydrogenase, branched-chain oxoacid dehydrogenase, and glycine cleavage protein[13]. It also acts as an accessory subunit of complex I with a 2:1 stoichiometry[14], and its knockdown in 293 T cells reduced complex I activity[13]. In addition, it participates in ironsulfur (FeS) biogenesis through interaction with and stabilization of the FeS biogenesis complex[15]. Because FeS centers are found in a number of subunits of electron transport chain (ETC) complexes I–III, it is possible that NDUFAB1 might also be crucial in the regulation of mitochondrial respiratory functions. Thus, NDUFAB1 might constitute a potential target to enhance mitochondrial metabolism.

In the present study, we demonstrate that NDUFAB1 is required for systemic glucose homeostasis and insulin signaling, and its overexpression protects mice against high-fat diet (HFD)-induced obesity and insulin resistance. Mechanistically, NDUFAB1 not only activates PDH in a lipoylation-dependent manner, but also promotes the assembly of respiratory complexes and supercomplexes. Collectively, our findings identify NDUFAB1 as a novel mitochondrial target to prevent obesity and insulin resistance through enhancing mitochondrial metabolism.

1. Materials and methods

1.1. Animal care and HFD treatment

All animal experiments were carried out following the rules of the Association for Assessment and Accreditation of Laboratory Animal Care (AAALAC) International and the *Guide for the Care and Use of Laboratory Animals* [National Institutes of Health (NIH), Bethesda, MD, USA]. All procedures were approved by the Animal Care Committee of Peking University accredited by AAALAC International (IMM-ChengHP-14).

Mice were housed under a 12-h light/dark cycle; food and water were provided *ad libitum*. For dietary intervention, from 3 wk of age, the male mice were fed an HFD (60% calories from fat) (D12492; Research Diets, New Brunswick, NJ, USA) or standard chow diet (11.4% calories from fat) (Academy of Military Medical Sciences, Beijing, China) as a control. The *db/db* diabetic mice were from Model Animal Research Center of Nanjing University (Nanjing, China).

1.2. Reagents and materials

Antibodies for NDUFAB1 and succinate dehydrogenase (SDH) complex flavoprotein subunit B were from OriGene Technologies (Rockville, MD, USA); antibodies for phosphorylated (p)–protein kinase B (Akt) and Akt were from Cell Signaling Technology (Danvers, MA, USA); antibodies for NDUFB8, SDHA, ubiquinol-cytochrome *c* reductase (UQCR)-C1, adenosine triphosphate (ATP) synthase, subunit b (ATPB), ATP synthase, subunit 5a (ATP5A), and lipoic acid were from Abcam (Cambridge, MA, USA); antibodies for NDUFS1, NDUFS6, UQCRFS1, cytochrome *c* oxidase (COX) IV, ironsulfur cluster assembly enzyme (ISCU), and NFS1 cysteine desulfurase (NFS1) were from ProteinTech (Wuhan, China); antibodies for dihydrolipoamide *S*-acetyltransferase and glyceraldehyde 3-phosphate dehydrogenase were from Abclonal Technology (Woburn, MA, USA). Other reagents were obtained commercially from MilliporeSigma (Burlington, MA, USA).

1.3. Generation of *Ndufab1* skeletal muscle–specific knockout mice

Floxed *Ndufab1* mice were generated by standard techniques using a targeting vector containing a neomycin (G418) resistance cassette flanked by Frt sites. Briefly, exon 3 of the *Ndufab1* gene was inserted into 2 flanking LoxP sites. After electroporation of the targeting vector into embryonic stem (ES) cells v.6.5 (129 × C57), G418-resistant ES cells were screened for homologous recombination by Southern blot. Two heterozygous recombinant ES clones were identified and microinjected into blastocysts from C57BL/6J mice to generate germline-transmitted floxed heterozygous mice (*Ndufab1*$^{f/+}$). Homozygous *Ndufab1*-floxed mice (*Ndufab1*$^{f/f}$) were obtained by inbreeding the *Ndufab1*$^{f/+}$ mice.

To generate skeletal muscle–specific *Ndufab1* knockout mice (mKO), *Ndufab1*$^{f/f}$ mice were bred with Mlc1f-Cre mice, in which Cre recombinase expression was controlled by the myosin light chain 1 promoter[16] to generate double heterozygous Mlc1f-Cre and *Ndufab1* floxed mice (Mlc1f-Cre/*Ndufab1*$^{f/+}$). The mice were then crossed with homozygous *Ndufab1*$^{f/f}$ mice or Mlc1f-Cre/*Ndufab1*$^{f/+}$ to generate Mlc1f-Cre^{+}/*Ndufab1*$^{f/f}$ as mKO, Mlc1f-Cre-/*Ndufab1*$^{f/f}$, with Mlc1f-Cre-/*Ndufab1*$^{f/+}$ mice as littermate controls (Supplemental **Figure S1A**). The mKO mice were born normally in Mendel ratio (Supplemental **Figure S1B**). Mice were genotyped by PCR using mouse tail DNA as well as flox primers (forward, 5'-ACAAATTCTCCCTGATGTCCTT-3'; reverse, 5'-TGTTCAACTTCATTTTGAGGTGGT-3') and Cre primers (forward, 5'-ATTGCTGTCACTTGGTCGTGGC-3'; reverse, 5'-GAAAATGCTTCTGTCCGTTTGC-3'), respectively.

1.4. Generation of *Ndufab1* pan-tissue transgenic mice

To generate pan-tissue transgenic mice expressing *Ndufab1*, the *Ndufab1* cDNA was cloned into the pCAGGS vector downstream of the chicken β-promotor. The construct was linearized with Hind III and Pvu I to release the transgenic cassette, purified with a DNA purification kit (Qiagen, Hilden, Germany) and micro- injected into fertilized eggs of C57BL/6J mice. The mice were genotyped by PCR using the primer 5'-AGCCTCTGCTAACCATGTTC-3' (forward) and 5'-GTCCAAACTGTCTAAGCCC-A-3' (reverse).

1.5. Histologic analysis

The gastrocnemius muscle, liver, white fat, and brown fat were fixed in 4% paraformaldehyde overnight at room temperature, embedded in paraffin, and serially sectioned with the thickness of 5 μm. Standard hematoxylin and eosin (HE) staining was performed on these sections. The adipocyte area of white fat and the lipid droplet area of brown fat were analyzed with ImageJ (NIH).

1.6. Measurement of whole-animal metabolic parameters

Mice were housed individually under a 12-h light/dark cycle. A comprehensive animal metabolic monitoring system (Clams; Columbus Instruments, Columbus, OH, USA) was used to evaluate oxygen consumption (VO_2) and carbon dioxide production (VCO_2) continuously over a 72-h period. The respiratory exchange ratio (RER) was calculated using the following formula: RER = VCO_2/VO_2. Energy expenditure was calculated using the following formula: energy expenditure = $(3.815 + 1.232\ VCO_2/VO_2) \times VO_2$. Spontaneous total activity of mice was monitored by a home-cage ambulatory activity test with an infrared sensor unit, measured as X + Y beam breaks over 12-h light-dark cycle.

In addition, the body fat mass and lean mass of animals were measured with a quantitative MRI (NMR) analyzer (EchoMRI, Houston, TX, USA).

1.7. Glucose tolerance test, insulin tolerance test, and blood and plasma analysis

Glucose tolerance test (GTT) was performed in 16-wk-old mice after they were deprived of food for 16 h. After measuring the basal blood glucose levels, the mice were intraperitoneally injected with D-glucose (2 g/kg

body weight); the blood glucose levels were then measured 15, 30, 60, 90, and 120 min after glucose injection. Insulin tolerance test (ITT) was performed in 16-wk-old mice with *ad libitum* feed. After measuring the basal blood glucose levels, the mice were intraperitoneally injected with bovine insulin (0.75 U/kg body weight; MilliporeSigma), and then the blood glucose levels were measured 15, 30, 60, 90, and 120 min after insulin injection. To analyze glucose-stimulated insulin release, after being unfed for 16 h, mice were injected intraperitoneally with D-glucose (2 g/kg), and the insulin concentrations were measured 15 and 30 min after glucose injection.

We collected blood *via* the tail vein before injection and at different time points after injection (as indicated in the figures). Blood glucose was measured using an AccuCheck blood glucose meter (Roche, Basel, Switzerland), and plasma insulin was measured using an ELISA kit (EZRMI-13K; MilliporeSigma). The serum triglyceride and cholesterol concentrations were measured using kits from Wako Diagnostics (Richmond, VA, USA) according to the manufacturer's instructions. The lactate concentration was measured using Amplite Fluorimetric D-Lactate Assay Kit from AAT Bioquest (Sunnyvale, CA, USA).

1.8. In vivo insulin signaling

The level of Akt phosphorylation in response to acute insulin stimulation in different organs was used to assess insulin signaling in vivo. Specifically, mice were unfed for 16 h and then given an intraperitoneal injection of insulin (1 U/kg body weight; MilliporeSigma). Fifteen minutes after injection, mice were euthanized *via* cervical dislocation, and the gastrocnemius muscle was collected, snap-frozen in liquid nitrogen, and kept at 280 °C until further analysis of Akt phosphorylation.

1.9. Isolation of flexor digitorum brevis cells and measurement of mitochondrial reactive oxygen species

For isolation of single muscle fibers, mice were euthanized by cervical dislocation, and the hind limbs were surgically removed and placed in Tyrode's solution containing 140 mM NaCl, 5 mM KCl, 10 mM 4-(2-hydroxyethyl)-1-piperazineethanesulfonic acid, and 2 mM $MgCl_2$ (pH 7.2). The flexor digitorum brevis (FDB) muscles were excised and transferred into Tyrode's solution supplemented with 0.2% type I collagenase for 70 min at 37 °C with shaking. After digestion, muscles were transferred into a 1.5 ml Eppendorf tube containing 600–700 ml of Tyrode solution supplemented with 2.5 mM $CaCl_2$. Muscle fibers were then gently dissociated by several passages through a small-diameter pipette. For measuring mitochondrial reactive oxygen species (ROS) of FDB cells, mitoSox (5 mM) was loaded at 37 °C for 30 min followed by 3 washes with Tyrode's solution. The mitoSox fluorescence was measured using an inverted confocal microscope (LSM 710; Carl Zeiss, Oberkochen, Germany) with a × 40, 1.3 numerical aperture oil-immersion objective by excitation at 514 nm and emission at 580–740 nm.

1.10. Transmission electron microscopy

The gastrocnemius muscles were isolated and dissected into 1–2 mm^3 blocks and immediately fixed with 2.5% glutaraldehyde and 4% paraformaldehyde, then postfixed with 1% osmium tetroxide. After dehydration in a graded series of acetone, the samples were embedded in Spurr resin and sectioned with a glass knife on a Leica Ultracut R cutter. Ultra-thin sections (70–90 nm) were imaged with a transmission electron microscope (Tecnai G2 20 Twin; Themo Fisher Scientific, Waltham, MA, USA). The images were analyzed using ImageJ to threshold and binarize the images, allowing quantification of the mitochondrial volume occupied by cristae according to the pixel percentage of cristae among total pixels.

1.11. Measurement of skeletal muscle mitochondrial respiration

Gastrocnemius muscles were washed with ice-cold isolation buffer [210 mM mannitol, 70 mM sucrose, 5 mM 4-(2-hydroxyethyl)-1-piperazineethanesulfonic acid (pH 7.4), 1 mM EGTA, and 1 mg/ml bovine serum

albumin], minced, and homogenized. The homogenate was centrifuged at 4 °C for 10 min at 700 *g*, and the supernatant was collected and further centrifuged at 4 °C for 10 min at 12,000 g. The mitochondrial pellet was resuspended for functional assessment. The protein concentration of the mitochondrial preparations was determined by NanoDrop Microvolume Spectrophotometer (Thermo Fisher Scientific). Mitochondrial respiration was evaluated by measuring oxygen consumption with a Clark-type oxygen electrode (Strathkelvin 782 2-Channel Oxygen System v.1.0; Strathkelvin Instruments, Motherwell, United Kingdom). Briefly, the isolated mitochondria were resuspended in respiration buffer (225 mM mannitol, 75 mM sucrose, 10 mM KCl, 10 mM Tris-HCl, 5 mM KH_2PO_4, pH 7.2) at 25 °C with different substrates added (malate/glutamate (2.5 mM each) for complex I, succinate (2.5 mM) for complex II, glycerol-3-phosphate (5 mM) for complex III, and ascorbate (2.5 mM)/*N*,*N*,*N*',*N*'-tetramethyl-p-phenylenediamine (0.5 mM) for complex IV). State II and III oxygen consumption rates (OCRs) were measured in the absence and presence of 100 μm ADP, respectively.

1.12. Measurement of PDH activity

The PDH activity was measured using the PDH activity colorimetric assay kit (BioVision, Milpitas, CA, USA). Briefly, 20 μg of isolated mitochondria from gastrocnemius muscle were resuspended in 50 μl PDH assay buffer, then 50 μl reaction mix (containing 46 ml PDH assay buffer, 2 μl PDH developer, and 2 μl PDH substrate) was added. The absorbance at 450 nm was measured immediately using Synergy HTX Multi-Mode Reader (BioTek, Winooski, VT, USA) in the kinetic mode for 60 min at 37 °C.

1.13. Blue native gel electrophoresis analysis of mitochondrial respiratory complexes and supercomplexes and in-gel activity analysis

Blue native gel electrophoresis (BNGE) was conducted using the NativePAGE system (Thermo Fisher Scientific). Briefly, the isolated gastrocnemius muscle mitochondria were solubilized by digitonin (4 g/g-protein) for 15 min on ice, followed by centrifugation at 15,000 rpm at 4 °C for 30 min. After centrifugation, the supernatants were collected and the protein concentration was determined by bicinchoninic acid analysis (Thermo Fisher Scientific). The Coomassie Blue G-250 (Thermo Fisher Scientific) was added to thesupernatants to obtain a dye/detergent massratio of 1:4, and then the protein was loaded into a 4–16% nondenaturing polyacrylamide gel (Thermo Fisher Scientific). After electrophoresis, proteins were transferred to a PVDF membrane (MilliporeSigma) and then probed with specific antibodies against subunits of complex I (NDUFB8), complex II (SDHA), complex III (UQCRFS1, UQCRC1), complex IV (COX IV), and complex V (ATPB). Blots were visualized using secondary antibodies conjugated with IRDye (Li-Cor Biosciences, Lincoln, NE, USA) and an Odyssey imaging system (Li-Cor Biosciences). The anti-NDUFB8, anti-UQCRC1, or anti-COX IV immunoblot bands with high MWs were used to reflect complex I-, complex III-, or complex IV-containing supercomplexes.

For in-gel activity analysis, 2.5 mg/ml nitro blue tetrazolium and 0.5 mg/ml NADH in 2 mM Tris-HCl (pH 7.4) were added to the 4–16% nondenaturing polyacrylamide gel after electrophoresis and incubated for 15 min at 37 °C. The reaction was stopped with 10% acetic acid. The activity was determined by analyzing the color development using the Odyssey Imaging System (Li-Cor Biosciences).

1.14. Western blot analysis

The tissues collected were immediately frozen in liquid nitrogen and stored at –80 °C until use. The tissues were homogenized with denaturinglysis buffer, and 80–100 μg of protein per sample was separated on 12% SDS-PAGE. After electrophoresis, proteins were transferred to a PVDF membrane and then probed with specific antibodies. Blots were visualized using secondary antibodies conjugated with IRDye and an Odyssey Imaging System as previously described.

For analyzing mitochondrial protein lipoylation level, the samples were separated on 12% SDS-PAGE. After electrophoresis, proteins were transferred to a PVDF membrane and then probed with a specific anti–lipoic acid antibody (ab58724; Abcam), which recognizes lipoic acid covalently attached to proteins. Blots were then visualized using secondary antibody conjugated with IRDye and an Odyssey imaging system as previously described.

1.15. Statistics

Data are expressed as means ± SEM. When appropriate, a Student's *t* test was applied to determine the statistical significance. The log-rank test was used for survival curves. A value of $P < 0.05$ was considered statistically significant.

2. Results

2.1. Skeletal muscle–specific ablation of NDUFAB1 disrupts glucose homeostasis

Because skeletal muscle is an important organ for whole-body glucose homeostasis[5,17–20], we constructed the mKO to explore the potential roles of NDUFAB1 in systemic metabolism (Supplemental **Figure S1A,B**). The protein level of NDUFAB1 was reduced by 84% in the skeletal muscle (**Figure 1A,B**) but showed little changes in other tissues of mKO mice (Supplemental **Figure S1C**). Surprisingly, compared with wild-type (WT) littermates (Mlc1f-Cre-/Ndufab1$^{f/f}$ or Mlc1f-Cre-/Ndufab1$^{f/+}$), the mKO mice exhibited smaller body size at birth (**Figure 1C**), growth arrest (**Figure 1D**), and early death within 5 postnatal days (**Figure 1E**). HE staining showed no significant structure changes of the skeletal muscle in mKO mice (Supplemental **Figure S1D**). However, although the mKO mice appeared to be breast-fed normally (**Figure 1C**), the blood glucose levels measured on d 3 were halved in mKO mice (**Figure 1F**), whereas the blood concentrations of triglyceride, cholesterol, and lactate were not significantly changed (Supplemental **Figure S2**). Consistently, the serum insulin levels were decreased by 59% in mKO mice (**Figure 1G**), and the glycogen contents in both skeletal muscle and liver were also significantly reduced (**Figure 1H,I**). Moreover, the phosphorylation of Akt at Ser473, which activates the insulin signaling pathway[21], was reduced in the skeletal muscle of mKO mice under basal condition (**Figure 1J,K**), in good agreement with the reduced blood glucose and insulin levels (**Figure 1F,G**). Altogether, these striking phenotypes in the mKO mice reveal a crucial role of NDUFAB1 in whole-body glucose homeostasis, growth, and survival in neonatal mice.

2.2. NDUFAB1 overexpression protects the mice against HFD-induced obesity and insulin resistance

A dramatic decrease of NDUFAB1 protein was detected in the skeletal muscle of both *db/db* diabetic mice (**Figure 2A**) and HFD-induced insulin resistance mice (**Figure 2B**), amid myriads of other changes, such as elevated serum glucose levels, and altered insulin signaling and gene expression[22,23]. This observation prompted us to hypothesize that such NDUFAB1 deficiency might represent a primal mitochondrial response to metabolic stress and thereby contribute to the vicious progression of systemic metabolic disorders that eventually lead to diabetes. In this regard, we reckoned that NDUFAB1 overexpression might be protective by counteracting metabolic stress-induced changes. To directly test this possibility, we generated pan-tissue *Ndufab1* transgenic mice (TG), in which NDUFAB1 was overexpressed by ~5.5 fold in the skeletal muscle (**Figure 2C**), ~2.0 fold in the white adipose tissue (Supplemental **Figure S3A**), ~4.3 fold in the brown adipose tissue (Supplemental **Figure S3B**), and ~5.0 fold in the liver (Supplemental **Figure S3C**) compared with control mice (WT). These mice from 3 wk of age on were challenged with metabolic stress induced by the HFD (60% calories from fat), and their body weight and metabolic parameters were then tracked for up to 16 wk. There were no significant differences in body weight between WT and TG mice when they were fed a chow

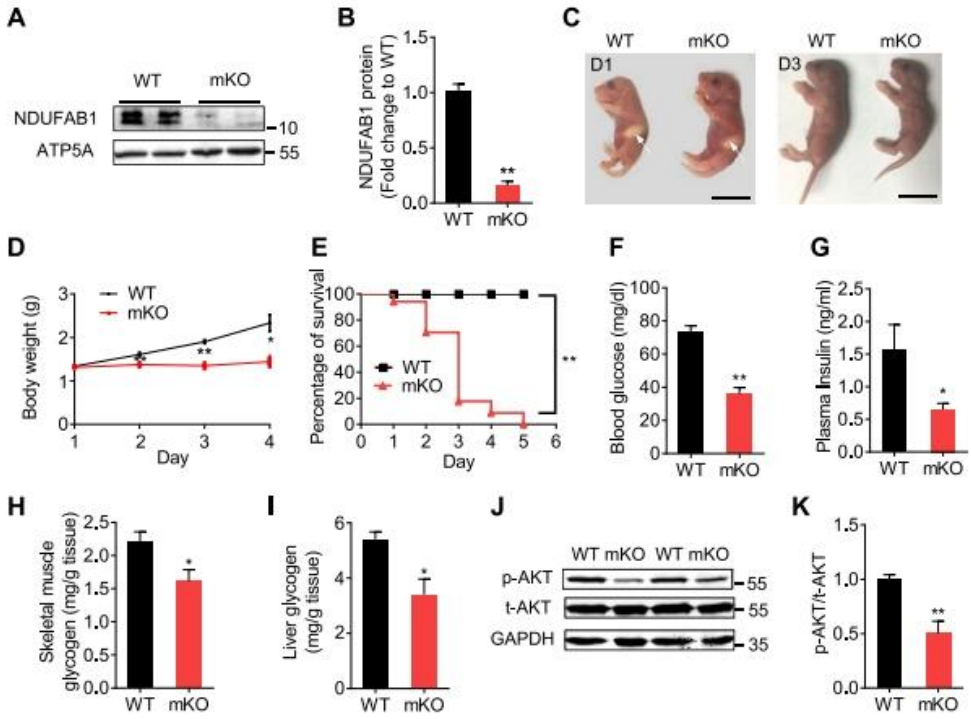

Figure 1. Skeletal muscle–specific ablation of NDUFAB1 causes impaired glucose homeostasis with early postnatal death. **(A)** Western blot of NDUFAB1 in the skeletal muscle of WT and mKO. Anti-ATP5A served as the loading control. **(B)** Quantification of NDUFAB1 protein levels in mKO vs. WT skeletal muscle from A. Data are means ± SEM; $n = 5$ mice/group. $^{**}P < 0.01$ mKO vs. WT. **(C)** Representative photos of WT and mKO mice at day (D)1 and D3 after birth. Scale bars, 1 cm. Note that the white arrows indicate that both WT and mKO mice have similar milk contents in their stomachs. **(D)** Body weight changes after birth. Data are means ± SEM; $n = 3$–12 mice/group. $^{*}P < 0.05$, $^{**}P < 0.01$ mKO *vs*. WT. **(E)** Kaplan–Meier survival curves of WT and mKO mice. Data are means ± SEM; $n = 33$ mice/group. $^{**}P < 0.01$ mKO *vs*. WT. **(F)** Blood glucose concentrations. In this and the following panels (**G–K**), data were obtained in WT and mKO mice at D3 and are presented as means ± SEM; $n = 14$ mice/group. $^{**}P < 0.01$ mKO *vs*. WT. **(G)** Plasma insulin concentrations. $n = 12$ mice/group; $^{*}P < 0.05$ mKO *vs*. WT. **(H)** Skeletal muscle glycogen content. $n = 4$ mice/group. $^{*}P < 0.05$ mKO *vs*. WT. **(I)** Liver glycogen content. $n = 6$ mice/group. $^{*}P < 0.05$ mKO *vs*. WT. **(J)** Western blot of Akt phosphorylation at Ser473 in skeletal muscle. **(K)** Fold change of Akt phosphorylation at Ser473 in mKO *vs*. WT mice. Data are means ± SEM; $n = 6$ mice/group. $^{**}P < 0.01$ mKO *vs*. WT.

diet (11.4% calories from fat) (**Figure 2D**). In WT mice, the body weight began to significantly rise after 5 wk on the HFD and reached a 49% increase after 13 wk on the HFD compared with the control group fed a chow diet (**Figure 2D**). By contrast, the TG mice showed significantly lower body weight from 9 wk on the HFD and reached only a 26% increase after 13 wk on the HFD (**Figure 2D**), suggesting a protective role for NDUFAB1 against HFD-induced obesity. Furthermore, NMR body composition analysis revealed that, as compared with WT mice on an HFD, TG mice on the HFD displayed significantly lower fat mass percentage but higher lean mass percentage (**Figure 2E,F**). With a chow diet, the blood cholesterol and triglyceride were not significantly changed between WT and TG mice (**Figure 2G,H**). After 13 wk on HFD, the elevation of blood cholesterol level was alleviated in TG *vs.* WT mice (**Figure 2H**), whereas triglyceride concentrations were similarly elevated in both groups (**Figure 2G**). Meanwhile, histologic analysis showed that TG mice showed decreased size of both visceral adipocytes (**Figure 2I** and Supplemental **Figure S3D**) and lipid droplets in brown fat (**Figure 2J** and Supplemental **Figure S3E**) and reduced hepatosteatosis (**Figure 2K**). All these results suggest that NDUFAB1 overexpression confers protection against HFD-induced metabolic disorders, evidenced by amelioration of HFD-induced obesity, disorder of fat metabolism, adipocyte hypertrophy, and hepatosteatosis.

Obesity occurs when the energy intake and expenditure are unbalanced. We then measured the caloric intake and energy expenditure with the metabolic monitoring system. Although the food intake was not significantly changed in the TG mice (**Figure 3A**), the energy expenditure together with oxygen consumption and CO_2 production was increased in TG *vs.* WT mice under the HFD at both light and dark phases (**Figure 3B–D**). The RER was

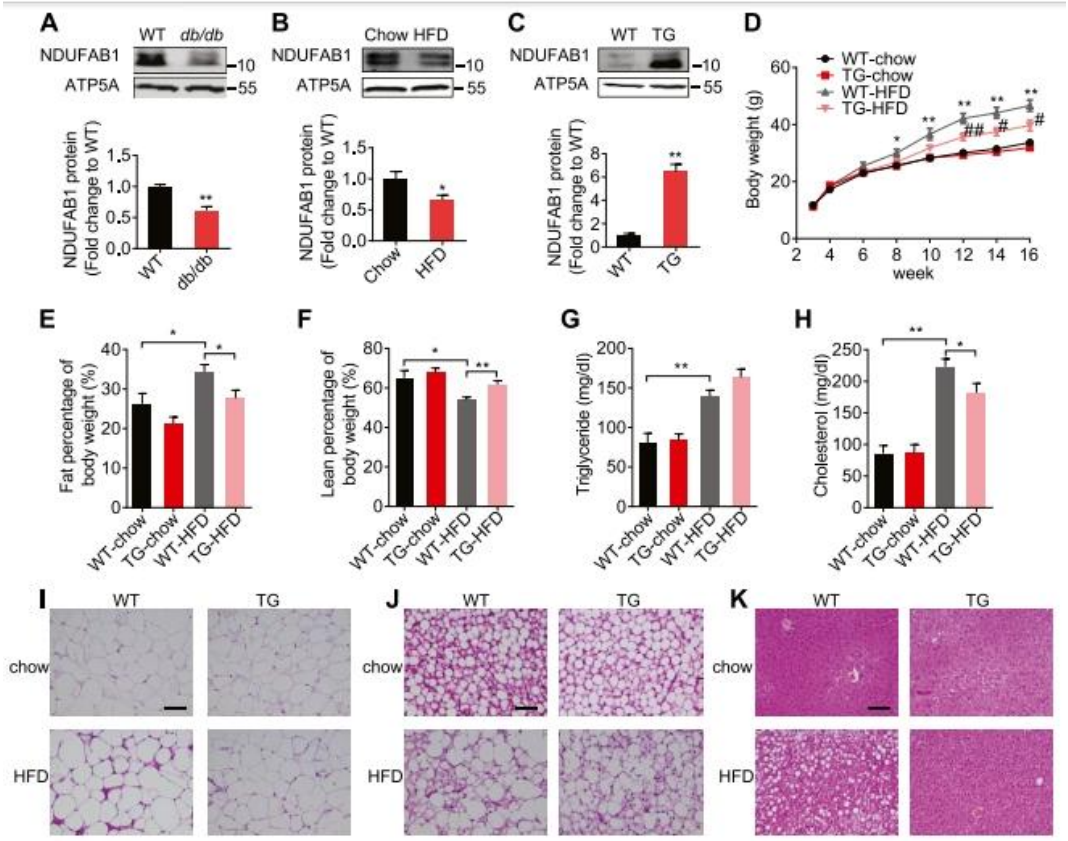

Figure 2. Amelioration of HFD-induced obesity and metabolic disorders in *Ndufab1* TG mice. **(A)** Western blot and corresponding fold change bar graph showing decreased NDUFAB1 protein levels in skeletal muscle of *db/db* mice. Data are means ± SEM; n =4 mice/group. ** $P < 0.01$ *db/db vs*. WT. **(B)** Western blot and corresponding fold change bar graph showing decreased NDUFAB1 protein levels in skeletal muscle of HFD-fed *vs*. standard chow diet (chow)-fed mice. Data are means ± SEM; n = 8 mice/group. *$P < 0.05$ HFD *vs*. chow diet. **(C)** Western blot of NDUFAB1 protein levels in the skeletal muscle of WT and Ndufab1 TG mice. Data are means ± SEM; n = 5–7 mice/group. **$P < 0.01$ TG *vs*. WT. **(D)** Body weight changes of WT and TG mice fed with the chow diet or the HFD. Data are means ± SEM; n = 6–11 mice/group. *$P < 0.05$, **$P < 0.01$ WT-HFD *vs*. WT-chow; *$P < 0.05$, **$P < 0.01$ TG-HFD *vs*. WT-HFD. **(E–H)** Fat mass **(E)**, lean mass **(F)**, blood triglyceride concentration **(G)**, and blood cholesterol concentration **(H)** in WT and TG mice after 13 wk of the standard chow diet or the HFD. Data are means ± SEM; n = 3–9 mice/group. *$P < 0.05$, **$P < 0.01$. **(I–K)** HE staining of white adipose **(I)**, brown adipose **(J)**, and liver **(K)** tissues from WT and TG mice fed with the chow diet or the HFD for 13 wk. Scale bars, 100 μm.

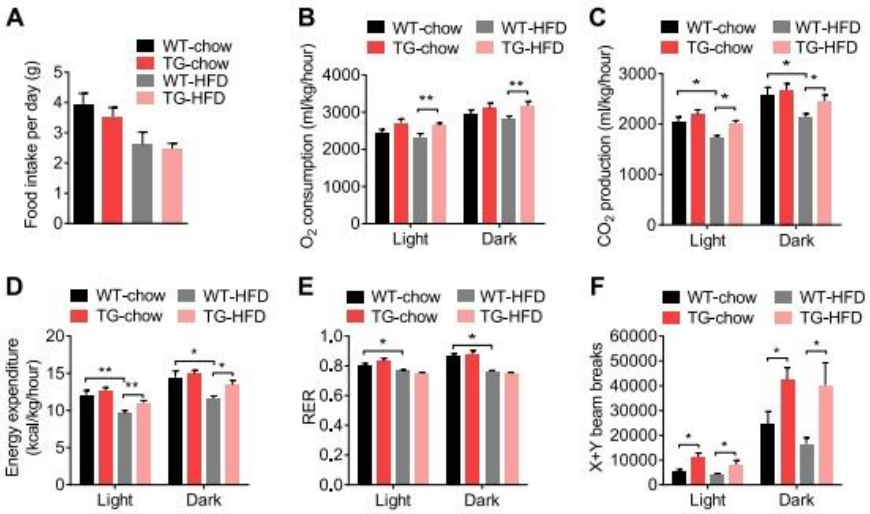

Figure 3. Systemic metabolic profiles in Ndufab1 TG mice. **(A)** Daily food intake of WT and TG mice fed with chow diet or HFD for 13 wk. Data are means ± SEM; n = 4–6 mice/group. **(B–F)** Oxygen consumption **(B)**, CO_2 production **(C)**, energy expenditure **(D)**, RER **(E)**, and home-cage activity (measured as X + Y beam breaks) **(F)** of WT and TG mice fed the chow diet or the HFD for 13 wk. Data are means ± SEM; n = 6–9 mice/group. *$P < 0.05$, **$P < 0.01$.

similar between WT and TG mice (**Figure 3E**), presumably because of the increase of both oxygen consumption and CO_2 production in the TG mice (**Figure 3B,C**). Moreover, TG mice showed a higher home-cage activity than WT mice (**Figure 3F**), which is suggestive of enhanced energy expenditure. To further assess the protective effect of NDUFAB1 overexpression on systemic metabolism, we performed GTT and ITT to detect possible changes in whole-body glucose metabolism and insulin sensitivity. As compared with WT groups, NDUFAB1 overexpression lowered concentrations of both fasting and fed blood glucose under the HFD and even fasting blood glucose under the chow diet (**Figure 4A**), dramatically enhanced glucose tolerance in both chow diet and HFD groups (**Figure 4B,C**), and enhanced insulin sensitivity in the HFD group (**Figure 4D,E**). In the HFD group, WT mice showed failure of glucose-stimulated insulin secretion (**Figure 4F,G**) associated with a 2.2-fold increase in basal insulin concentrations (**Figure 4F**), but TG mice showed unaltered insulin baseline levels and a normal insulin secretion response to glucose stimulation (**Figure 4F,G**). As to insulin signaling *in vivo*, the Akt phosphorylation at Ser473 in skeletal muscle of TG mice in response to insulin stimulation was significantly elevated compared with that in WT mice, under either chow diet or HFD conditions (**Figure 4H,I**). Altogether, these results reveal that NDUFAB1 overexpression effectively protects the mice against HFD-induced obesity and insulin resistance.

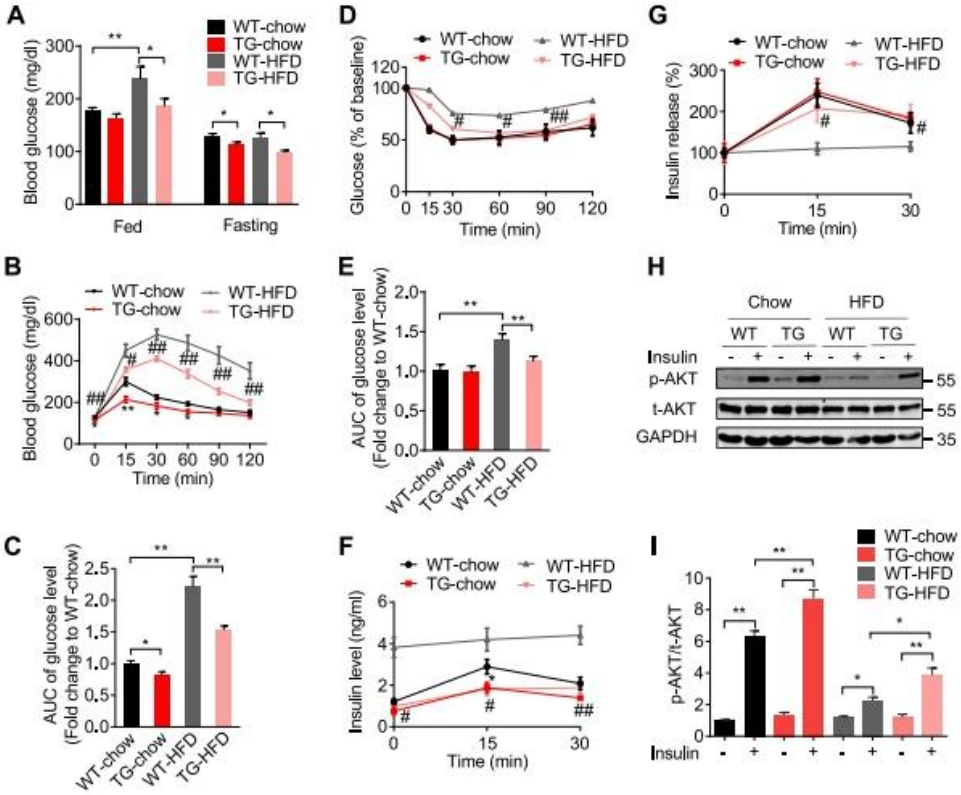

Figure 4. NDUFAB1 overexpression protects the mice against HFD-induced insulin resistance. **(A)** Blood glucose concentrations at fed and unfed states of WT and TG mice. Data are means ± SEM; n = 7–10 mice/group. *P < 0.05, **P < 0.01. **(B)** GTT in WT and TG mice. Data are means ± SEM; n = 7–9 mice/group. *P < 0.05, **P < 0.01 TG-chow diet *vs*. WT-chow diet; *P < 0.05, **P < 0.01 TG-HFD *vs*. WT-HFD. **(C)** Analysis of the area under the curve (AUC) of GTT. Data are means ± SEM; n = 7–9 mice/group. *P < 0.05, **P < 0.01. **(D)** ITT in WT and TG mice. Data are means ± SEM; n = 9–10 mice/group. *P < 0.05, **P < 0.01 TG-HFD *vs*. WT-HFD. **(E)** Analysis of the AUC of ITT. Data are means ± SEM; n = 9–10 mice/group. **P < 0.01. **(F,G)** Glucose (2 g/kg body weight, i.p.) stimulated changes in serum insulin concentrations **(F)** or their relative changes indicated as percentage of the respective baselines **(G)**. Data are means ± SEM; n = 7–9 mice/group. *P < 0.05 TG-chow diet *vs*. WT-chow diet. *P < 0.05, **P < 0.01 TG-HFD *vs*. WT-HFD. **(H)** Western blot of Akt phosphorylation at Ser473 stimulated by insulin (1 U/kg body weight, intraperitoneally injected) in skeletal muscle. **(I)** Fold change of Akt phosphorylation at Ser473. Data are means ± SEM; n = 5–8 mice/group. *P < 0.05, **P < 0.01. All the experiments were performed in male mice fed the chow diet or the HFD for 13 wk.

2.3. NDUFAB1 regulates PDH lipoylation and activation in the skeletal muscle

To dissect the molecular mechanisms whereby NDUFAB1 overexpression protects against metabolic stress, we

first examined the possible involvement of the NDUFAB1-mediated mtFAS pathway[11,12] by measuring mitochondrial protein lipoylation status because lipoic acids synthesized by mtFAS serve as a cofactor of many enzymes, including PDH, aketoglutarate dehydrogenase, and the branched-chain oxoacid dehydrogenase[13]. Interestingly, we found that lipoylation of the PDH E2 subunit was significantly reduced in the skeletal muscle of d 3 mKO mice (**Figure 5A,B**), and enzymatic activity analysis showed a 52% reduction in mKO skeletal muscle (**Figure 5C**), supporting the essential role of NDUFAB1-regulated lipoylation in PDH activation. Interestingly, the lipoylation of PDH E2 subunit was dramatically increased in skeletal muscle of TG mice under both chow diet and HFD (**Figure 5D,E**), and the PDH activity was enhanced by 35% under the chow diet and 20% under the HFD in the skeletal muscle of TG mice (**Figure 5F**). Moreover, when challenged by HFD, the PDH activity was significantly reduced in WT mitochondria from skeletal muscle (**Figure 5F**), suggesting the involvement of PDH inactivation in the development of insulin resistance. These results suggest that NDUFAB1-regulated lipoylation and activation of mitochondrial metabolic enzymes participate in the protection against metabolic stress.

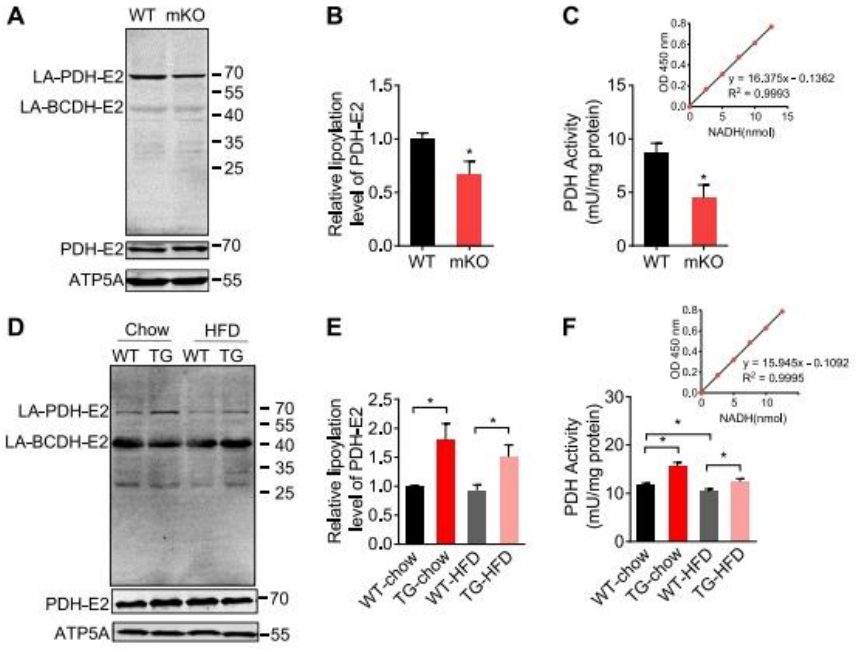

Figure 5. Effects of NDUFAB1 alteration on PDH lipoylation and activation. **(A)** Western blot of mitochondrial protein lipoylation status in skeletal muscle of d 3 WT and mKO mice. LA-PDH-E2, lipoic acid-conjugated E2 subunit of pyruvate dehydrogenase; LA-BCDH-E2, lipoic acid-conjugated E2 subunit of branched-chain oxoacid dehydrogenase E2. Anti-ATP5A served as the loading control. **(B)** Relative lipoylation levels from the Western blot in A. Data are means ± SEM; $n = 7$ mice/group. *$P < 0.05$ mKO *vs*. WT. **(C)** PDH activity in skeletal muscle mitochondria of d 3 WT and mKO. The inset panel shows the standard curve. Data are means ± SEM; $n = 5$ mice/group. *$P < 0.05$ mKO *vs*. WT. **(D)** Western blot of mitochondrial protein lipoylation status in skeletal muscle of WT and TG mice fed the chow diet or the HFD. Anti-ATP5A served as the loading control. **(E)** Relative mitochondrial protein lipoylation status from *D*. Data are means ± SEM; $n = 5$–7 mice/group. *$P < 0.05$. **(F)** Enhanced PDH activity in the skeletal muscle mitochondria of TG mice. Data are means ± SEM; $n = 3$–5 mice/group. *$P < 0.05$.

2.4. NDUFAB1 enhances mitochondrial respiration, reduces ROS, and facilitates the assembly of respiratory complexes and supercomplexes in the skeletal muscle

Next, we assessed changes of mitochondrial morphology with electron microscopy. We found disrupted cristae structure and greater mitochondrial volume devoid of the cristae in mKO skeletal muscle (**Figure 6A,B**). Although the cristae structure was not significantly changed in TG skeletal muscle (Supplemental **Figure S4A,B**), we detected a 45% reduction of the ROS level in FDB cells from TG animals (**Figure 6C,D**). Moreover, we analyzed the impact of NDUFAB1 ablation and overexpression on mitochondrial respiration in the presence of different substrates. The state III OCRs in mKO mitochondria was significantly decreased with either complex I substrate, complex II substrate, or complex III substrate but was not altered with complex IV substrate (**Figure**

6E). In contrast, the TG mitochondria showed higher state III OCRs in the presence of all complex I–III substrates under both chow diet and HFD, whereas the complex IV substrate-supported state III OCR was not significantly changed (**Figure 6F–I**). Moreover, HFD decreased the state III OCRs in the presence of all substrates of complexes I–IV in WT mitochondria (**Figure 6F–I**). The state II OCRs were not significantly changed in mKO mitochondria (Supplemental **Figure S4C**) and TG mitochondria (Supplemental **Figure S4D–G**). These results indicate that NDUFAB1 bidirectionally regulates mitochondrial respiration in accordance with its expression level and implicate that NDUFAB1 is a highly viable target for manipulation of mitochondrial metabolism.

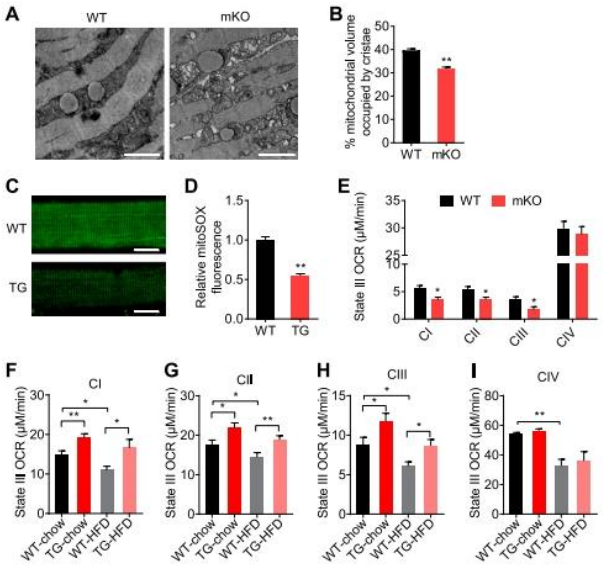

Figure 6. Altered mitochondrial respiration in skeletal muscle of mKO and TG mice. **(A)** Representative electron microscopy structure of skeletal muscle mitochondria from WT and mKO mice. Scale bars, 2 μm. **(B)** Quantification of mitochondrial volume occupied by cristae. Data are means ± SEM; n = 68–74 mitochondria from 3 mice/group. $^{**}P < 0.01$ *vs*. WT. **(C**, **D**) Decreased mitochondrial ROS level in TG FDB cells. **(C)** Representative mitoSoX fluorescence images of WT and TG FDB cells. Scale bar, 20 μm. **(D)** Quantification of mitoSoX fluorescence normalized to WT. Data are means ± SEM; n = 45–70 cells from 3 male mice. $^{**}P < 0.01$ *vs*. WT. **(E)** Decreased state III OCR in the mitochondria from mKO skeletal muscle *vs*. WT. The OCRs were measured in the presence of different substrates: malate/glutamate (Mala/Glu) for complex I, succinate (Succ) for complex II, glycerol-3-phosphate (G3P) for complex III, and ascorbate (Asc)/N,N,N',N'-tetra-methyl-p-phenylenediamine (TMPD) for complex IV, along with ADP. Data are means ± SEM; n = 5–7, d 3 mice/group. $^{*}P < 0.05$ *vs*. WT. **(F–I)** Changes of state III OCR in TG mitochondria. As listed in **(E)**, different respiratory substrates were used for complex I **(F)**, complex II **(G)**, complex III **(H)**, and complex IV **(I)**. Data are means ± SEM; n = 3–8 mice/group. $^{*}P < 0.05$, $^{**}P < 0.01$.

To further interrogate the molecular mechanisms underlying NDUFAB1's effect on mitochondrial respiration, we measured the abundance of ETC complexes. We also placed an emphasis on the assembly of supercomplexes because the formation of supercomplexes of different composition and stoichiometry has been shown to enhance the electron transfer efficiency and reduce ROS production[24–28]. In-gel activity analysis showed that the activity of complex I and supercomplexes was decreased significantly in mKO mitochondria (**Figure 7A**), whereas in TG mitochondria, their activity was enhanced (**Figure 7B**). BNGE followed by Western blot analysis showed that, in mKO mitochondria, the contents of complexes I, II, and III were significantly decreased, whereas that of complex IV was unchanged (**Figure 7C**). Moreover, NDU-FAB1 ablation dramatically reduced the contents of supercomplexes containing complex I, III, or IV (**Figure 7C**). In contrast, NDUFAB1 overexpression significantly increased the contents of complex I and the aforementioned supercomplexes under both the chow diet and the HFD (**Figure 7D,E**). That is, NDUFAB1 deficiency impaired the assembly of individual respiratory complexes I–III, as well as the subsequent supercomplexes, whereas NDUFAB1 overexpression enhanced the assembly of complex I and supercomplexes.

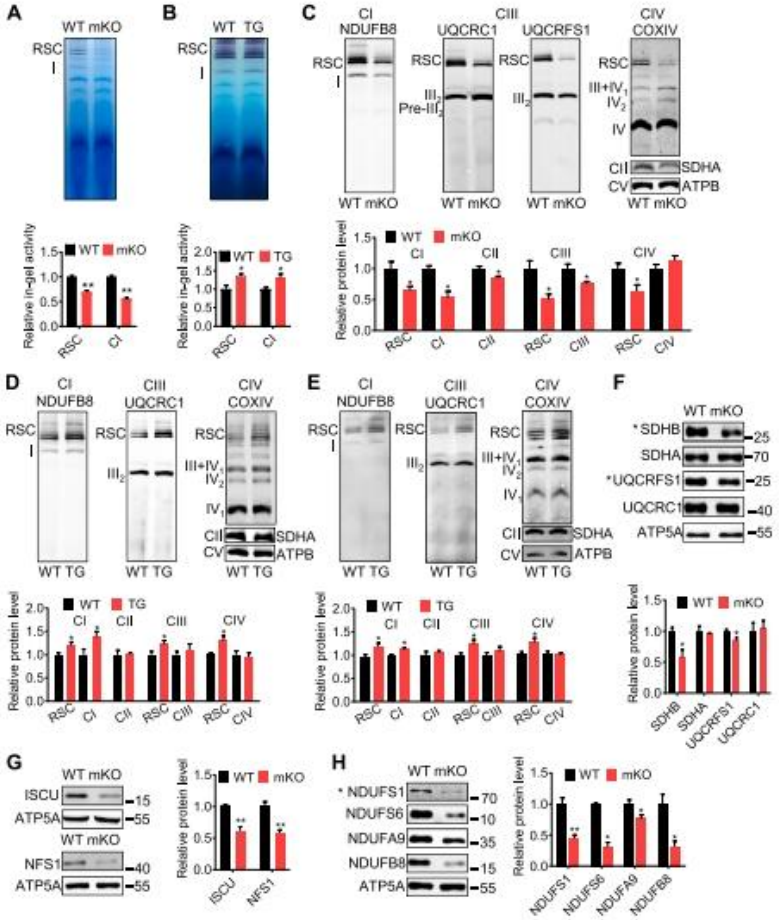

Figure 7. Essential role of NDUFAB1 in the assembly of respiratory complexes and supercomplexes (RSC) in the skeletal muscle. **(A)** Reduced in-gel activity of RSC and complex I in mKO mitochondria. Data are means ± SEM (lower panel); $n = 5$, d 3 mice/group. $^{**}P < 0.01$ mKO *vs*. WT. **(B)** Enhanced in-gel activity of RSC and complex I in TG mitochondria. Data are means ± SEM (lower panel); $n = 5$–7 mice/group; $^{*}P < 0.05$ TG *vs*. WT. **(C)** BNGE immunoblots of respiratory complexes and RSC in the skeletal muscle of d 3 WT and mKO mice. The supercomplexes were visualized by antibodies against subunits of complex I (CI, NDUFB8), complex III (CIII, UQCRC1 or UQCRFS1), and complex IV (CIV, COX IV). Complex II (CII) was visualized by antibody against SDHA, and complex V (CV) with antibody against ATPB. Data are means ± SEM (lower panel); $n = 4$–5, d 3 mice/group. $^{*}P < 0.05$ mKO *vs*. WT. **(D, E)** BNGE immunoblots of the respiratory complexes and RSC in WT and TG skeletal muscle. The mice were fed the standard chow diet (**D**) or the HFD (**E**) for 13 wk. Data are means ± SEM (lower panels); $n = 6$–9 mice/group **(D)**; $n = 7$–9 mice/group **(E)**. $^{*}P < 0.05$ TG *vs*. WT. **(F)** Western blot of CII and CIII subunits. Asterisk denotes FeS-containing subunits. Anti-ATP5A served as the loading control. Data are means ± SEM (lower panel); $n = 4$, d 3 mice/group. $^{*}P < 0.05$ mKO *vs*. WT. **(G)** Western blot of ISCU and NFS1. Anti-ATP5A served as the loading control. Data are means ± SEM (right panel); $n = 8$, d 3 mice/group. $^{**}P < 0.01$ mKO *vs*. WT. **(H)** Western blot of CI subunits. Asterisk denotnes FeS-containing subunits. Anti-ATP5A served as the loading control. Data are means ± SEM (right panel); $n = 4$, d 3 mice/group. $^{*}P < 0.05$, $^{**}P < 0.01$ mKO *vs*. WT.

Furthermore, we measured the contents of individual subunits of complexes I–III. We found that only the FeS-containing subunits, SDHB of complex II and UQCRFS1 of complex III, were significantly decreased in the absence of NDUFAB1 (**Figure 7F**). Notably, there was accumulation of an intermediate assembly of complex III, which lacks UQCRFS1, an FeS-containing subunit that is incorporated at the last step[29], in mKO mitochondria (**Figure 7C**). These results indicate that NDUFAB1 ablation selectively disrupts FeS-containing subunits of complex II and complex III. Moreover, ISCU and NFS1, 2 important components of the FeS biogenesis complex[30,31], were significantly down-regulated in mKO skeletal muscle (**Figure 7G**). These results suggest that FeS assembly is a driving factor for NDUFAB1's role on mitochondrial respiration. For complex I, however, a different pattern emerged: all its examined subunits, whether FeS-containing (NDUFS1) or not (NDUFS6, NDUFB8, NDUFA9), were decreased in mKO mitochondria (**Figure 7H**). This result is consistent with the fact that NDUFAB1 is an important accessory subunit of complex I, with 2 copies positioned at NDUFA6 and NDUFB9[14], and suggests that NDUFAB1 might regulate complex I assembly by enhancing the interaction of different subunits.

Hence, NDUFAB1 critically regulates the assembly of complexes I–III through its dual roles of an FeS biogenesis regulator and a complex I subunit. Nonetheless, despite the increased complex I assembly, the contents of individual subunits of complex I as well as those of complexes II and III were not significantly changed in TG mitochondria (Supplemental **Figure S5A,B**).

These asymmetric effects of NDUFAB1 ablation and overexpression suggest that the abundance of endogenous NDUFAB1 might be sufficient for the stability of these subunits in TG mitochondria. In this regard, NDUFAB1 overexpression enhances mitochondrial respiration, likely by enhancing formation of complex I and supercomplexes.

3. Discussion

In the present study, we have provided direct evidence that NDUFAB1 is crucial for systemic glucose metabolism and insulin signaling. Skeletal muscle–specific knockout of *Ndufab1* caused severe hypoglycemia and hypoinsulinemia as well as defective Akt signaling and depletion of glycogen storage in multiple organs and tissues, leading to postnatal growth arrest and early death. More importantly, pan-tissue NDUFAB1 overexpression effectively protected the mice against HFD-induced obesity and insulin resistance with enhanced energy expenditure associated with increased home-cage activity. These results not only underscore the intimate linkage of mitochondrial metabolism to whole-body metabolism and even behavioral change but also reveal an essential role of NDUFAB1 in maintaining glucose homeostasis. As such, we have also demonstrated that NDUFAB1 constitutes an attractive target to protect against metabolic stress by boosting mitochondrial metabolism.

As a multifunctional mitochondrial protein, NDUFAB1 regulates mitochondrial metabolism at the junction of multiple pathways. First of all, as the acyl carrier protein[32], it regulates the lipoylation status of PDH through mtFAS[13]. MtFAS was discovered decades ago[11,12], but its physiologic and pathologic importance has not been fully appreciated. Here, we revealed a new role of mtFAS in systemic metabolism through regulation of PDH lipoylation. The mitochondrial PDH complex acts as a central metabolic node that mediates pyruvate oxidation after glycolysis and fuels the Krebs cycle to meet energy demands[33]. It has been previously shown that post-translational modifications of PDH subunits, including phosphorylation and de-phosphorylation, acetylation, and succinylation, regulate PDH activity[33]. The present study shows that NDUFAB1-mediated lipoylation of the PDH E2 subunit constitutes another important post-translational modification to regulate its activity. In the absence of NDUFAB1, lipoylation of the PDH E2 subunit is largely repressed, resulting in reduced PDH activity. On the other hand, NDUFAB1 over-expression enhances PDH activity by elevating its lipoylation. Because the reduction of PDH lipoylation is associated with the development of obesity and insulin resistance induced by the HFD, it is tempting to propose that this post-translational modification might be a novel etiology in metabolic disorders.

Another major finding of this study is that NDUFAB1 enhances mitochondrial metabolism by promoting the assembly of ETC complexes I–III and supercomplexes. In the absence of NDUFAB1, the assembly of complexes I–III and the resultant supercomplexes were severely impaired in skeletal muscle mitochondria. Importantly, only the FeS-containing subunits of complexes II and III were selectively down-regulated, and a premature complex III lacking the FeS-containing subunit UQCRFS1 accumulated in mKO mitochondria. Together with the reduction of ISCU and NFS1 in the skeletal muscle of mKO mice, these results support a crucial role of NDUFAB1 in FeS biogenesis for the assembly of complexes I–III. As NDU-FAB1 is also a complex I subunit with 2 copies critically positioned for intersubunit interactions[34], NDUFAB1 appears to affect the stability of all complex I subunits, including those lacking FeS clusters. Thus, NDUFAB1 regulates the assembly of respiratory complexes and supercomplexes through its dual roles of as a regulator of FeS biogenesis and as a

complex I subunit.

The formation of supercomplexes are thought to channel electron transfer more efficiently, limit ROS production, protect vulnerable electron transfer chain sites in the complexes from oxidative damage, and stabilize individual complexes[26,35–41]. Particularly, supercomplexes have been shown to dynamically adapt to changes in cellular metabolism[42–45], and impaired supercomplex assembly has been identified in the skeletal muscle of diabetic obese individuals[46]. Our findings further support the notion that enhanced respiratory supercomplex formation by NDUFAB1 overexpression can confer protection against metabolic stress induced by the HFD.

The striking phenotypes of mKO were somewhat unexpected. Multiple possible mechanisms might be at work. First, reduced PDH lipoylation and impaired assembly of respiratory complexes and supercomplexes in the mKO mice should directly disrupt mitochondrial metabolism of skeletal muscle, switching the muscle energy metabolism to rely more on glycolysis and generating different intermediate metabolites, which may enter circulation and affect downstream targets not only in skeletal muscle but also other tissues, including the liver, fat, and the insulin-secretory pancreas. Second, considering the important role of NDUFAB1 in FeS biogenesis[15], it is also possible that NDUFAB1 ablation in the skeletal muscle may dysregulate whole-body iron homeostasis. In consistence, a previous report has shown that knockout of transferrin receptor in skeletal muscle led to iron deficiency in muscles and lowered blood glucose and insulin[47]. Persistent hypoglycemia and hypo-insulinemia may underlie the retarded growth of neonatal mKO mice, and the early death may be consequential to severely dysregulated glucose and iron homeostasis. However, we cannot exclude the involvement of other interorgan communication mechanisms or yet-to-be-identified targets of NDUFAB1.

It should be cautioned that, although we focused on the skeletal muscle in our mechanistic investigation of the protective metabolic phenotypes of the TG mice, we don't exclude roles of other tissues, such as liver and fat, in contributing to the protection against HFD-induced metabolic stress. To the contrary, given that NDUFAB1 is ubiquitous among different cell types, we believe its pan-tissue over-expression should be beneficial to boost mitochondrial metabolism in many organs, making it a more appealing target for combating metabolic stress. Because the skeletal muscle is the largest organ for metabolism, the enhanced mitochondrial metabolism induced by NDUFAB1 over-expression in skeletal muscle likely constitutes a major contributor to the metabolic protection in the TG mice.

Our findings reveal that NDUFAB1 effectively protects against metabolic stress by coordinately enhancing activities of PDH and ETC. Particularly, NDUFAB1 regulates PDH activity through modulation of lipoylation of its E2 subunit in an mtFAS-dependent manner. Meanwhile, it modulates ETC activity through regulation of the assembly of complexes I–III and supercomplexes. Taken together, our findings identify the multifunctional mitochondrial protein NDUFAB1 as a promising target to boost mitochondrial metabolism for the treatment of metabolic disorders.

Acknowledgments

The authors thank Dongwei Ma for histology, Dr. Xiaowei Chen for providing Mlc1f-Cre mice, and Drs. Yan Zhang and Ruiping Xiao (all from the Institute of Molecular Medicine) for valuable comments. This work was supported by the National Key Basic Research Program of China (2017YFA0504000 and 2016YFA0500403) and the National Science Foundation of China (31470811, 31670039, 8182780030, and 31821091). The authors declare no conflicts of interest.

Author contributions

R. Zhang and T. Hou designed and performed the experiments; and H. Cheng and X. Wang designed the experiments and wrote the manuscript.

Abbreviations

ATP, adenosine triphosphate; BNGE, blue native gel electrophoresis; ES, embryonic stem; ETC, electron transport chain; FDB, flexor digitorum brevis; FeS, iron-sulfur; GTT, glucose tolerance test; HE, hematoxylin and eosin; HFD, high-fat diet; ISCU, FeS cluster assembly enzyme; ITT, insulin tolerance test; mKO, skeletal muscle–specific *Ndufab1* knockout mice; mtFAS, mitochondrial fatty acid synthesis; NDU, NADH: ubiquinone oxidoreductase; OCR, oxygen consumption rate; PDH, pyruvate dehydrogenase; RER, respiratory exchange ratio; ROS, reactive oxygen species; TG, *Ndufabl* transgenic mice; NFS1, NFS1 cysteine desulfurase; SDH, succinate dehydrogenase; UQCR, ubiquinol-cytochrome *c* reductase; $\dot{V}CO_2$, carbon dioxide production; $\dot{V}O_2$, oxygen consumption; WT, wild type.

References

1. Boyle JP, Thompson TJ, Gregg EW, et al. Projection of the year 2050 burden of diabetes in the US adult population: Dynamic modeling of incidence, mortality, and prediabetes prevalence. *Population Health Metrics* 2010; 8: 29. doi: 10.1186/1478-7954-8-29
2. Johnson AMF, Olefsky JM. The origins and drivers of insulin resistance. *Cell* 2013; 152(4): 673–684. doi: 10.1016/j.cell.2013.01.041
3. Muoio DM. Metabolic inflexibility: When mitochondrial indecision leads to metabolic gridlock. *Cell* 2014; 159(6): 1253–1262. doi: 10.1016/j.cell.2014.11.034
4. Szendroedi J, Phielix E, Roden M. The role of mitochondria in insulin resistance and type 2 diabetes mellitus. *Nature Reviews Endocrinology* 2012; 8: 92–103. doi: 10.1038/nrendo.2011.138
5. Hesselink MKC, Schrauwen-Hinderling V, Schrauwen P. Skeletal muscle mitochondria as a target to prevent or treat type 2 diabetes mellitus. *Nature Reviews Endocrinology* 2016; 12: 633–645. doi: 10.1038/nrendo.2016.104
6. Sivitz WI, Yorek MA. Mitochondrial dysfunction in diabetes: From molecular mechanisms to functional significance and therapeutic opportunities. *Antioxidants & Redox Signaling* 2010; 12(4): 537–577. doi: 10.1089/ars.2009.2531
7. Kraegen EW, Cooney GJ, Turner N. Muscle insulin resistance: A case of fat overconsumption, not mitochondrial dysfunction. *Proceedings of the National Academy of Sciences* 2008; 105(22): 7627–7628. doi: 10.1073/pnas.0803901105
8. Erion DM, Shulman GI. Diacylglycerol-mediated insulin resistance. *Nature Medicine* 2010; 16: 400–402. doi: 10.1038/nm0410-400
9. Pagel-Langenickel I, Bao J, Pang L, Sack MN. The role of mitochondria in the pathophysiology of skeletal muscle insulin resistance. *Endocrine Reviews* 2010; 31(1): 25–51. doi: 10.1210/er.2009-0003
10. Runswick MJ, Fearnley IM, Skehel JM, Walker JE. Presence of an acyl carrier protein in NADH: Ubiquinone oxidoreductase from bovine heart mitochondria. *FEBS Letters* 1991; 286(1–2): 121–124. doi: 10.1016/0014-5793(91)80955-3
11. Hiltunen JK, Chen Z, Haapalainen AM, et al. Mitochondrial fatty acid synthesis—An adopted set of enzymes making a pathway of major importance for the cellular metabolism. *Progress in Lipid Research* 2010; 49(1): 27–45. doi: 10.1016/j.plipres.2009.08.001
12. Feng D, Witkowski A, Smith S. Down-regulation of mitochondrial acyl carrier protein in mammalian cells compromises protein lipoylation and respiratory complex I and results in cell death. *Journal of Biological Chemistry* 2009; 284(17): 11436–11445. doi: 10.1074/jbc.M806991200
13. Brody S, Oh C, Hoja U, Schweizer E. Mitochondrial acyl carrier protein is involved in lipoic acid synthesis in Saccharomyces cerevisiae. *FEBS Letters* 1997; 408(2): 217–220. doi: 10.1016/S0014-5793(97)00428-6
14. Vinothkumar KR, Zhu J, Hirst J. Architecture of mammalian respiratory complex I. *Nature* 2014; 515(7525): 80–84. doi: 10.1038/nature13686
15. Van Vranken JG, Jeong MY, Wei P, et al. The mitochondrial acyl carrier protein (ACP) coordinates mitochondrial fatty acid synthesis with iron sulfur cluster biogenesis. *Elife* 2016; 5: e17828. doi: 10.7554/eLife.17828
16. Lyons GE, Ontell M, Cox R, et al. The expression of myosin genes in developing skeletal muscle in the mouse embryo. *The Journal of Cell Biology* 1990; 111(4): 1465–1476. doi: 10.1083/jcb.111.4.1465
17. Shulman GI, Rothman DL, Jue T, et al. Quantitation of muscle glycogen synthesis in normal subjects and subjects with non-insulin-dependent diabetes by ^{13}C nuclear magnetic resonance spectroscopy. *New England Journal of Medicine* 1990; 322(4): 223–228. doi: 10.1056/NEJM199001253220403
18. DeFronzo RA, Gunnarsson R, Björkman O, et al. Effects of insulin on peripheral and splanchnic glucose metabolism in noninsulin-dependent (type II) diabetes mellitus. *The Journal of Clinical Investigation* 1985; 76(1): 149–155. doi: 10.1172/JCI111938

19. DeFronzo RA, Jacot E, Jequier E, et al. The effect of insulin on the disposal of intravenous glucose: Results from indirect calorimetry and hepatic and femoral venous catheterization. *Diabetes* 1981; 30(12): 1000–1007. doi: 10.2337/diab.30.12.1000
20. Petersen KF, Dufour S, Savage DB, et al. The role of skeletal muscle insulin resistance in the pathogenesis of the metabolic syndrome. *Proceedings of the National Academy of Sciences* 2007; 104(31): 12587–12594. doi: 10.1073/pnas.0705408104
21. Petersen MC, Shulman GI. Mechanisms of insulin action and insulin resistance. *Physiological Reviews* 2018; 98(4): 2133–2223. doi: 10.1152/physrev.00063.2017
22. Nesteruk M, Hennig EE, Mikula M, et al. Mitochondrial-related proteomic changes during obesity and fasting in mice are greater in the liver than skeletal muscles. *Functional & Integrative Genomics* 2014; 14: 245–259. doi: 10.1007/s10142-013-0342-3
23. Zhang F, Xu X, Zhang Y, et al. Gene expression profile analysis of type 2 diabetic mouse liver. *PloS One* 2013; 8(3): e57766. doi: 10.1371/journal.pone.0057766
24. Wu M, Gu J, Guo R, et al. Structure of mammalian respiratory supercomplex I1III2IV1. *Cell* 2016; 167(6): 1598–1609. doi: 10.1016/j.cell.2016.11.012
25. Sousa JS, Mills DJ, Vonck J, Kühlbrandt W. Functional asymmetry and electron flow in the bovine respirasome. *Elife* 2016; 5: e21290. doi: 10.7554/eLife.21290
26. Letts JA, Fiedorczuk K, Sazanov LA. The architecture of respiratory supercomplexes. *Nature* 2016; 537: 644–648. doi: 10.1038/nature19774
27. Gu J, Wu M, Guo R, et al. The architecture of the mammalian respirasome. *Nature* 2016; 537: 639–643. doi: 10.1038/nature19359
28. Guo R, Zong S, Wu M, et al. Architecture of human mitochondrial respiratory megacomplex I2III2IV2. *Cell* 2017; 170: 1247–1257. doi: 10.1016/j.cell.2017.07.050
29. Wagener N, Ackermann M, Funes S, Neupert W. A pathway of protein translocation in mitochondria mediated by the AAA-ATPase Bcs1. *Molecular Cell* 2011; 44(2): 191–202. doi: 10.1016/j.molcel.2011.07.036
30. Maio N, Rouault TA. Iron–sulfur cluster biogenesis in mammalian cells: New insights into the molecular mechanisms of cluster delivery. *Biochimica et Biophysica Acta (BBA)-Molecular Cell Research* 2015; 1853(6): 1493–1512. doi: 10.1016/j.bbamcr.2014.09.009
31. Roche B, Aussel L, Ezraty B, et al. Reprint of: Iron/sulfur proteins biogenesis in prokaryotes: Formation, regulation and diversity. *Biochimica et Biophysica Acta (BBA)-Bioenergetics* 2013; 1827(8–9): 923–937. doi: 10.1016/j.bbabio.2013.05.001
32. Brody S, Mikolajczyk S. Neurospora mitochondria contain an acyl-carrier protein. *European Journal of Biochemistry* 1988; 173(2): 353–359. doi: 10.1111/j.1432-1033.1988.tb14005.x
33. Park S, Jeon JH, Min BK, et al. Role of the pyruvate dehydrogenase complex in metabolic remodeling: Differential pyruvate dehydrogenase complex functions in metabolism. *Diabetes & Metabolism Journal* 2018; 42: 270–281. doi: 10.4093/dmj.2018.0101
34. Fiedorczuk K, Letts JA, Degliesposti G, et al. Atomic structure of the entire mammalian mitochondrial complex I. *Nature* 2016; 538: 406–410. doi: 10.1038/nature19794
35. Porras CA, Bai Y. Respiratory supercomplexes: Plasticity and implications. *Frontiers in Bioscience (Landmark Edition)* 2015; 20: 621–634. doi: 10.2741/4327
36. Milenkovic D, Blaza JN, Larsson NG, Hirst J. The enigma of the respiratory chain supercomplex. *Cell Metabolism* 2017; 25(4): 765–776. doi: 10.1016/j.cmet.2017.03.009
37. Maranzana E, Barbero G, Falasca AI, et al. Mitochondrial respiratory supercomplex association limits production of reactive oxygen species from complex I. *Antioxidants & Redox Signaling* 2013; 19: 1469–1480. doi: 10.1089/ars.2012.4845
38. Lopez-Fabuel I, Le Douce J, Logan A, et al. Complex I assembly into supercomplexes determines differential mitochondrial ROS production in neurons and astrocytes. *Proceedings of the National Academy of Sciences* 2016; 113(46): 13063–13068. doi: 10.1073/pnas.1613701113
39. Schägger H, de Coo R, Bauer MF, et al. Significance of respirasomes for the assembly/stability of human respiratory chain complex I. *Journal of Biological Chemistry* 2004; 279(35): 36349–36353. doi: 10.1074/jbc.M404033200
40. Acín-Pérez R, Bayona-Bafaluy MP, Fernández-Silva P, et al. Respiratory complex III is required to maintain complex I in mammalian mitochondria. *Molecular Cell* 2004; 13(6): 805–815. doi: 10.1016/S1097-2765(04)00124-8
41. Diaz F, Fukui H, Garcia S, Moraes CT. Cytochrome *c* oxidase is required for the assembly/stability of respiratory complex I in mouse fibroblasts. *Molecular and Cellular Biology* 2006; 26(13): 4872–4881. doi: 10.1128/MCB.01767-05
42. Lapuente-Brun E, Moreno-Loshuertos R, Acín-Pérez R, et al. Supercomplex assembly determines electron flux in the mitochondrial electron transport chain. *Science* 2013; 340(6140): 1567–1570. doi: 10.1126/science.123038

43. Guaras A, Perales-Clemente E, Calvo E, et al. The $CoQH_2$/CoQ ratio serves as a sensor of respiratory chain efficiency. *Cell Reports* 2016; 15: 197–209. doi: 10.1016/j.celrep.2016.03.009
44. Acin-Perez R, Enriquez JA. The function of the respiratory supercomplexes: The plasticity model. *Biochimica et Biophysica Acta (BBA)-Bioenergetics* 2014; 1837(4): 444–450. doi: 10.1016/j.bbabio.2013.12.009
45. Greggio C, Jha P, Kulkarni SS, et al. Enhanced respiratory chain supercomplex formation in response to exercise in human skeletal muscle. *Cell Metabolism* 2017; 25: 301–311. doi: 10.1016/j.cmet.2016.11.004
46. Antoun G, McMurray F, Thrush AB, et al. Impaired mitochondrial oxidative phosphorylation and supercomplex assembly in rectus abdominis muscle of diabetic obese individuals. *Diabetologia* 2015; 58: 2861–2866. doi: 10.1007/s00125-015-3772-8
47. Barrientos T, Laothamatas I, Koves TR, et al. Metabolic catastrophe in mice lacking transferrin receptor in muscle. *EBioMedicine* 2015; 2(11): 1705–1717. doi: 10.1016/j.ebiom.2015.09.041